Origin of intense blue-green emission in $SrTiO_3$ thin films with implanted nitrogen ions: An investigation by synchrotron-based experimental techniques

Vishnu Kumar,[1,*] Anuradha Bhogra,[2] Manju Bala,[1] S. C. Haw,[3] C. L. Chen,[3] C. L. Dong,[4] K. Asokan,[2,†] and S. Annapoorni[1,‡]

[1]*Department of Physics and Astrophysics, University of Delhi, Delhi, 110007, India*
[2]*Inter-University Accelerator Centre, Aruna Asaf Ali Marg, New Delhi, 110067, India*
[3]*National Synchrotron Radiation Research Center, Hsinchu, 30076, Taiwan*
[4]*Department of Physics, Tamkang University, Tamsui 25137, Taiwan*

(Received 2 February 2020; revised 8 November 2020; accepted 15 December 2020; published 12 January 2021)

The present study utilizes synchrotron-based x-ray diffraction (XRD), photoluminescence (PL), and x-ray absorption near edge structure (XANES) spectroscopic techniques to comprehend the evolution of optical intense blue-green emission in 100 keV nitrogen (N) ion implanted $SrTiO_3$ (STO) thin films deposited by RF magnetron sputtering technique. The XRD pattern shows a shift in reflections at lower N ion fluences and the amorphization of the films at higher fluences. A disordered phase induced by implantation in the STO films leads to an intense blue-green emission due to oxygen (O) vacancies and N ($2p$) bound states. A schematic diagram of energy levels has been proposed to explain the origin of PL emission. The XANES spectra at Ti K edge reflect a change in the valency of Ti ions and the local atomic structure of ordered and disordered phases of STO with an increase in N ion fluence. The splitting of peak assigned to e_g orbitals, and discrepancy in ratio $d_{z^2}/d_{x^2-y^2}$ observed in the Ti L- and O K-edge spectra, confirm a distortion in TiO_6 octahedral structure and modifications in O $2p$-Ti $3d$ hybridization states. The synchrotron-based techniques reveal that N ion implanted STO can be a good photoluminescent material exhibiting a variety of emissions through bound states of O vacancies and implanted N ions.

DOI: 10.1103/PhysRevB.103.024104

I. INTRODUCTION

Perovskite oxide materials with ABO_3 type structure are employed in a wide range of applications including photocatalytic activity, semiconductor devices, optoelectronic devices, and also used as an insulating layer in most electronic devices [1–6]. A well-known prototype perovskite compound, $SrTiO_3$ (STO) shows a cubic structure at room temperature and is widely used as photocatalyst for dye degradation on ultraviolet light (UV) irradiation [7]. It is well known that pure crystalline STO does not show any photoluminescence (PL) emission at room temperature under UV light, but a broad emission is observed at low temperatures [8,9]. Blue light emission at room temperature was first reported by Kan *et al.* due to O vacancies induced by 300 keV argon (Ar^+) ion irradiation in STO thin films [10]. In another study, Kumar *et al.* irradiated STO single crystals with 550 eV Ar^+ ions and showed three distinct PL emissions: ∼430 nm, ∼550 nm, and ∼830 nm [11]. These studies show that the optical properties can be modified or improved by introducing defects in the material. Despite extensive study on the electrical properties and electronic structures of STO, the origin of photoluminescence and its correlation with band structure and induced defect states remains unclear. Therefore, the role of defects in modifying the optical properties like PL is very intriguing and is a very important subject of study [5,12]. Defects can be produced during the synthesis of materials or created by several modifications induced by external parameters like thermal treatment [13,14] and ion beam irradiation or implantation etc. [15]. Controlling the defects to produce desired variation in the properties of semiconductors is a challenging task. Ion beam implantation technique has widely revolutionized physical properties especially optical and electrical nature of the material [10,15]. It can induce charge carriers, defects, lattice distortion, vacancies, and trap levels in the material up to the desired depth with a reproducible precise dose that plays a crucial role in improving the functionality of transition metal oxides [10,16]. This technique not only produces the oxygen (O) vacancies and defects but also can introduce self-doping of the ions in interstitial sites such as O or Ti interstitials [17]. These interstitials modify the structural and optical properties of materials [18]. Nitrogen (N) ions can occupy O sites resulting in transition metal oxynitrides [19]. The hybridized states of N ($2p$) are slightly at higher potential energy than that of O ($2p$) [20]. Correlation between defects and electronic structures have been studied using x-ray photoelectron spectroscopy (XPS) [18], electron paramagnetic resonance (EPR) [21,22], and x-ray absorption spectroscopy (XAS) [5,23,24]. However, there are very few detailed investigations of fundamental changes in the photoluminescence properties of STO films induced by N ion implantation.

*vkmevphysics@gmail.com
†asokaniuac@gmail.com
‡annapoornis.phys@gmail.com

The present study employs the synchrotron-based characterization techniques to investigate the effect of 100 keV N ion implantation on the structural, optical properties, and electronic structures of STO and also meticulously attempts to correlate the origin of optical emissions with introduced defects and modified electronic structure. Based on experimental observation, N ion implanted STO can be perceived as good photoluminescent material. The observed emissions are comprehended by x-ray absorption near-edge structure (XANES) studies and further corroborated by literature related to the first principle calculations and explained using schematic diagram of energy levels of STO comprising localized bound states of O vacancies and N 2*p* levels.

II. EXPERIMENTAL DETAILS

STO thin films were deposited on quartz substrates using a commercial STO target of 2 mm thickness and 5 cm diameter by radio frequency (RF) magnetron sputtering (HIND HIVAC, Model 12" MSPT) in the presence of oxygen (20%) balanced with argon gas. The cleaned quartz substrates of dimensions 10 mm × 10 mm × 2 mm were used to deposit STO thin films. The vacuum chamber was maintained at $\sim 5 \times 10^{-6}$ mbar before deposition. The plasma was processed at a fixed power of 250 W. During the deposition, a mixture of argon (Ar) and oxygen (O_2) (20%) gas was circulated into the chamber maintaining the pressure of $\sim 5 \times 10^{-2}$ mbar. The substrates were kept at room temperature and exposed to the plasma for 40 min. These films were annealed at 750 °C for 5 h in a horizontal tubular furnace in Ar+O_2 (20%) gas flow controlled using a needle valve and the gas was effluent through the water. Hereafter, these samples are considered as "Pristine" films. These pristine films were implanted with 100 keV N ion beam at room temperature using the low energy ion beam facility (LEIBF) housed in Inter-University Accelerator Centre (IUAC), New Delhi with different fluences viz. $\sim 5 \times 10^{14}$, $\sim 1 \times 10^{15}$, $\sim 5 \times 10^{15}$, and $\sim 1 \times 10^{16}$ ions/cm^2 and these samples are hereafter referred as N-5E14, N-1E15, N-5E15, and N-1E16, respectively. The time for irradiation was estimated using the parameters; ion beam current (nA), sample area (cm^2), and the fluence of the ion beam (number of incident ions/cm^2) in the equation (1).

$$\text{Time (sec)} = \frac{\text{Fluence} \times \text{Area}}{\text{Current} \times 6.25 \times 10^9} \quad (1)$$

For the structural characterization, synchrotron glancing incidence x-ray diffractometer (GIXRD) operated at 13 keV was used at MCX Beamline, Elettra Sincrotrone Trieste, Italy [25,26]. The x-ray source was fixed at a glancing angle of 0.2° and the detector was rotated with a step size of 0.01° to record the intensity of reflections in the 2θ range from 18° to 45°. Further, the samples were characterized by synchrotron PL spectroscopy at TLS-03A1, and XAS at TLS-20A1 & TLS-17C1 beamlines of National Synchrotron Radiation Research Center (NSRRC), Hsinchu, Taiwan. The PL measurements were performed at room temperature in a vacuum chamber ($\sim 10^{-7}$ Torr) in reflection mode at an incident angle of ~45° of the source beam with the sample. The intensity of PL emissions was measured by using a Photomultiplier Tube (PMT detector; Hamamatsu R943–02) operated at 1700 V and kept at an angle of 90° with respect to the beam [27,28]. The emission spectra were collected under excitation with 240 nm. During these measurements, an optical filter was used to remove band emissions from the spectra. Soft XAS measurements were carried out at 20A1 beamline in a vacuum chamber ($\sim 10^{-7}$ Torr) and the spectra were recorded in total electron yield (TEY) mode. XAS measurements with hard x rays were performed in air using a sample rotator at 17 C1 Wiggler beamline and spectra were recorded in fluorescence mode. Thickness measurements were performed using Rutherford backscattering (RBS) spectrometry at IUAC New Delhi. TRIM (Transport of Ions in Matter) and SRIM (The Stopping and Range of Ions in Matter) simulations were used to determine the ion beam parameters like range, electronic and nuclear stopping power, and straggling.

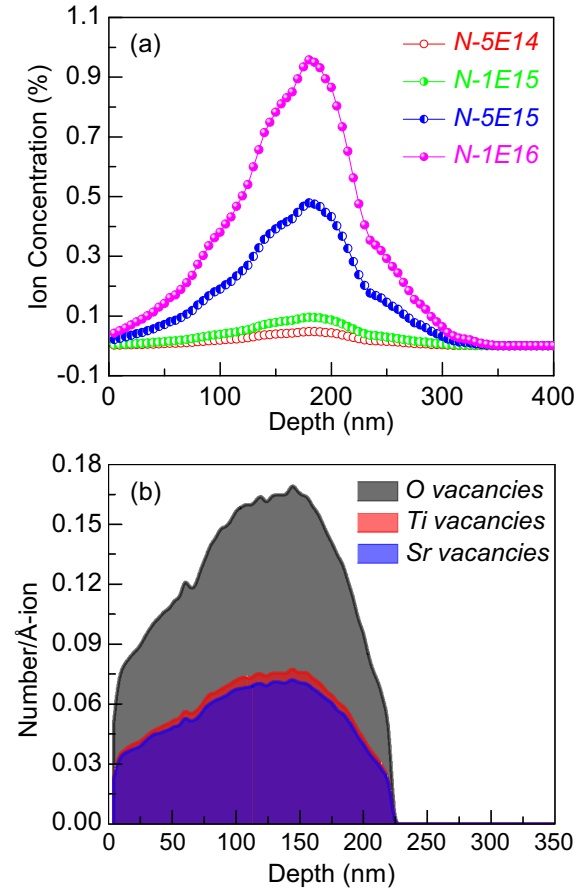

FIG. 1. (a) Calculated N ion concentration in STO thin films corresponding to different ion fluences and (b) the possible Ti, Sr, and O vacancies simulated by TRIM in the 225 nm STO thin films on quartz substrate.

III. RESULTS

The plots of ion energy versus energy loss and the depth versus energy loss are shown in Fig. A (see Supplemental Material, SM [29]) along with other parameters derived from SRIM-TRIM simulations. The maximum N ion concentrations were calculated to be 0.05%, 0.1%, 0.5%, and 0.9% in N-5E14, N-1E15, N-5E15, and N-1E16, respectively

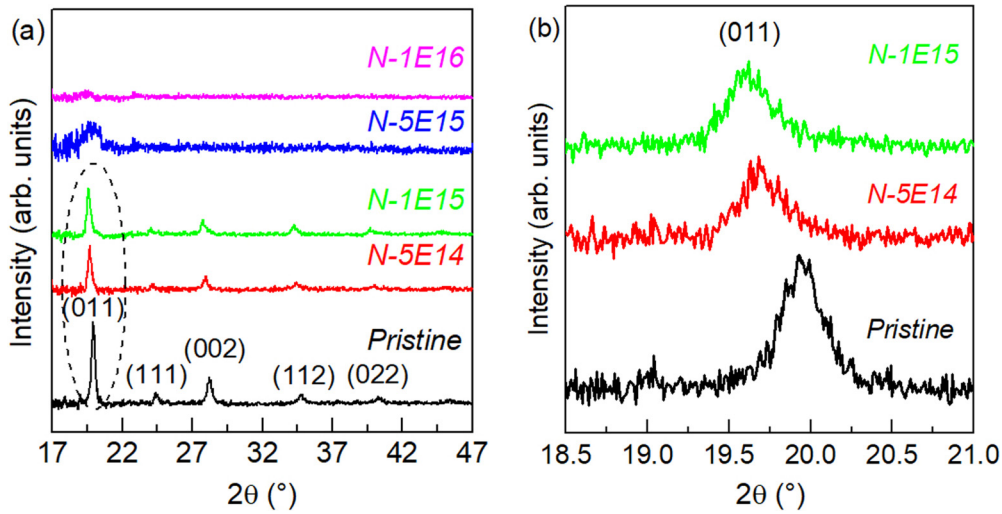

FIG. 2. XRD spectra of STO thin films: (a) pristine, N-5E14, N-1E15, N-5E15, and N-1E16 and (b) closer view of x-ray peak resulting from the diffraction of the (011) plane of pristine, N-5E14, and N-1E15.

[Fig. 1(a)], and the Sr, Ti, and O vacancies were estimated to be 0.070, 0.075, and 0.165 number/Å-ion using TRIM calculations [Fig. 1(b)]. The unit "per Å" is used in order to keep the numerical values as small numbers on the plot. The unit "numbers/ion" stands for the number of vacancies created in the material per incident ion [30] (see SM for other descriptions [29]). The thickness of as-grown films was estimated to be ∼220 nm by RBS. The RBS spectra and corresponding depth profile of pristine and N-1E16 are shown in Fig. B (see SM [29]).

Figure 2(a) shows the GIXRD spectra of pristine, N-5E14, N-1E15, N-5E15, and N-1E16. The observed reflections of pristine match well with the standard data (High Score Plus reference number 98-002-3076) of cubic perovskite polycrystalline structure of STO. The lattice parameters were calculated to be ∼3.905 Å for pristine STO film. Figure 2(b) compares the XRD peaks resulting from the diffraction of the (011) plane for the three samples: Pristine, N-5E14, and N-1E15. The x-ray peaks corresponding to (011) planes in the XRD pattern for N-5E14 and N-1E15 show a shift of 0.21° and 0.28°, respectively, towards lower angle, ascertaining an expansion in the unit cell of STO. The lattice parameters a, b, and c were calculated to be 3.947 Å, 3.938 Å, and 3.951 Å for N-5E14, and 3.969 Å, 3.948 Å, and 3.973 Å for N-1E15, respectively. A slight expansion along all axes is observed after N ion implantation. XRD spectra of N-5E15 and N-1E16 indicate that higher ion fluences result in amorphization of the samples (discussed later). The interplanar spacing (d-spacing) values calculated using the Bragg's equation for the corresponding plane (hkl) are found increasing with N ion fluences (see Table I).

The modification in crystal structure leads to the changes in optical properties. To identify the possible optical emissions due to defects created by N ion implantation, the PL measurements were performed for all the samples. No significant emission intensity was observed for the pristine sample as seen from Fig. 3 and this is consistent with the literature [9,10,31].

The PL spectra of N-5E14, N-1E15, N-5E15, and N-1E16 were fitted using Origin 8.6 software with three distinct Gaussian peaks. The position, standard error, and FWHM of the Gaussian peaks are presented in Table II and the figures, illustrating deconvolutions are shown in Fig. C (see SM [29]). In the inset of Fig. 3, a typical deconvolution process is shown for N-5E14 and N-1E16. All N ion-implanted samples have two common peaks at ∼415 nm (A) and ∼550 nm (D). Apart from these peaks, N-5E14 and N-1E15 have a peak at ∼480 nm (C), and N-5E15 and N-1E16 have at ∼460 nm (B). Peak C appears at lower fluence, which shifts towards lower wavelength at higher fluences and is assigned as peak B. All these peaks, at ∼415 nm (blue), ∼460 nm (blue), ∼480 nm (blue), and ∼550 nm (green), correspond to the energy of ∼2.98 eV, ∼2.69 eV, ∼2.58 eV, and ∼2.25 eV, respectively. An enhancement in the PL intensity is observed for all emissions with an increase in the ion fluence. This result is consistent with the study by Pontes *et al.* which reported an intense PL emission at room temperature in amorphous STO thin films [32].

A broad PL emission corresponds to a convolution of multiple transitions involving various energy levels. Moreover, it is affected by the defects, Fermi level, density of states, etc. All these factors contribute to the broadening of the

TABLE I. "d spacing" for corresponding planes (hkl) of pristine and N-5E14, and N-1E15.

	Pristine		N-5E14		N-1E15	
hkl	2θ (°)	d (Å)	2θ (°)	d (Å)	2θ (°)	d (Å)
011	19.90	2.7606	19.69	2.7897	19.62	2.7996
111	24.43	2.2553	24.17	2.2783	24.06	2.2886
002	28.23	1.9559	27.94	1.9758	27.81	1.9849
112	34.80	1.5942	34.45	1.6108	34.29	1.6180
022	40.39	1.3807	39.95	1.3963	39.77	1.4023
013	45.42	1.2348	45.07	1.2446	44.78	1.2522

TABLE II. The fitting parameters (in nm) of PL spectra of N ion implanted STO thin films.

	N-5E14		N-1E15		N-5E15		N-1E16	
Peak	Position	FWHM	Position	FWHM	Position	FWHM	Position	FWHM
A	415.29 ± 0.30	44.72	414.03 ± 0.27	43.74	413.85 ± 0.14	43.19	413.91 ± 0.09	42.40
B					463.18 ± 1.53	79.89	462.90 ± 1.83	87.71
C	483.53 ± 1.10	77.67	482.28 ± 1.22	82.36				
D	555.10 ± 6.30	159.87	553.24 ± 4.23	167.73	551.73 ± 8.93	153.03	546.33 ± 7.87	150.52

experimental PL spectra [33]. The transitions at lower wavelengths are more populated than that of higher wavelengths. Consequently, the blue emission is sharper than the greenish emission. The latter emission is more significant at higher fluences where an increased number of N ions causes the local amorphization leading to the rise of the extended VB and CB along with the tailing localized states [34,35]. The FWHM of these emissions increases with an increase in the wavelength (see Table II). The formation of tailing localized states provides a path to the excited electrons to emit the photons through various defects levels. This results in a broad range of the emission which is centered at a defined energy, i.e., the center of the Gaussian peak, where the emissions are maximum for a particular peak. Moreover, the strong electron-phonon coupling may lead to dissipation of some energy of the excited electrons and this may also cause variation in the energy of emitted photons [36–38].

The PL emission of N ion implanted STO films indeed suggests the presence of defects, interstitials, and vacancies but does not give any explicit evidence regarding any specific type of defect. The synchrotron GIXRD, on one hand, reveals the effect of the N ion implantation on the average crystal structure and shift in the reflections followed by amorphization. The evolution of PL is attributed to the possible O vacancies, lower crystallinity, and ion-beam induced defects. The localized studies based on the electronic states of elements may help to verify the aforementioned proposition. Hence, XANES at Ti K edge was studied to examine the local environment of Ti ions. The Ti K-edge features appear due to the transition of $1s$ core electrons to the unoccupied states consisting of $3d$ and $4sp$ orbitals strongly hybridized with the O $2p$ orbitals above the Fermi level, E_f.

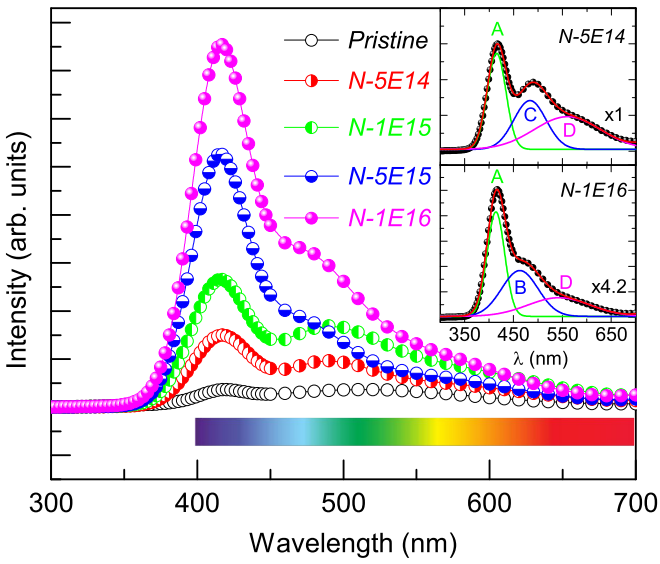

FIG. 3. Photoluminescence spectra of STO thin films: pristine, N-5E14, N-1E15, N-5E15, and N-1E16. The spectra were recorded under excitation with 240 nm and the band emission was eliminated using an optical filter during the measurements. Inset shows a typical deconvolution process for N-5E14 and N-1E16. Note that the blue-green emission evolves on N ion implantation.

The XANES spectra at Ti K edge for the STO thin films of pristine, N-5E14, N-1E15, N-5E15, and N-1E16 STO thin films are shown in Fig. 4(a). The spectra were normalized using Athena software [39]. The pre-edge features of all the films consist of two peaks appearing in the energy range of ∼4966 eV to 4972 eV. The features were deconvoluted using two Gaussian functions. The inset shows a magnified view of the pre-edge region and a representative deconvolution of pristine is shown under the curve. The pre-edge peaks are attributed to the transitions to unoccupied $3d$ t_{2g} and $3d$ e_g states. The e_g peaks are marked as α in Fig. 4(a). The fitting parameters of the peak are shown in Table III. The peak α departs to the lower energy with an increase in ion fluence. Figure 4(b) shows the change in the position and intensity of the peak α by varying the N ion fluence. To analyze the trend of the variation of pre-edge peak parameters with the change in N ion fluence, one needs to understand the origin of this peak.

The pre-edge features appear just above the Fermi level E_f and below the main absorption edge due to the transition of electrons from $1s$ to $3d$ t_{2g} and $3d$ e_g orbitals. These transitions are forbidden by the dipole selection rules since these involve a change in the orbital angular momentum $\triangle L = 2$ [40]. The experimental observation of pre-edge features is a consequence of the fact that the final state of photoelectrons possesses an admixture of p-d characters via the hybridization of Ti $3d$ and O $2p$ orbitals [40,41]. Therefore, the change in intensity and position of the peaks suggests the modification in degree of hybridization after N ion implantation.

Based on experimental analysis of Ti K edge along with multiple scattering calculations, Farges *et al.* [40] and Frenkel *et al.* [41,42] related the position and intensity of pre-edge peaks with the coordination number, oxidation state, and off-center displacement of Ti ions [40–42]. Farges *et al.* compared the experimental and theoretical data to provide the physics involved in pre-edge region and to distinguish between the fivefold, and mixture of fourfold and sixfold coordinated Ti ions (cf. Fig. 2 in Ref. [40]). The changes in local environment of Ti ions are expected to be reflected in the pre-edge of XANES spectra in terms of variation in the intensity and position of peaks [43,44]. The larger intensity of peak corresponds

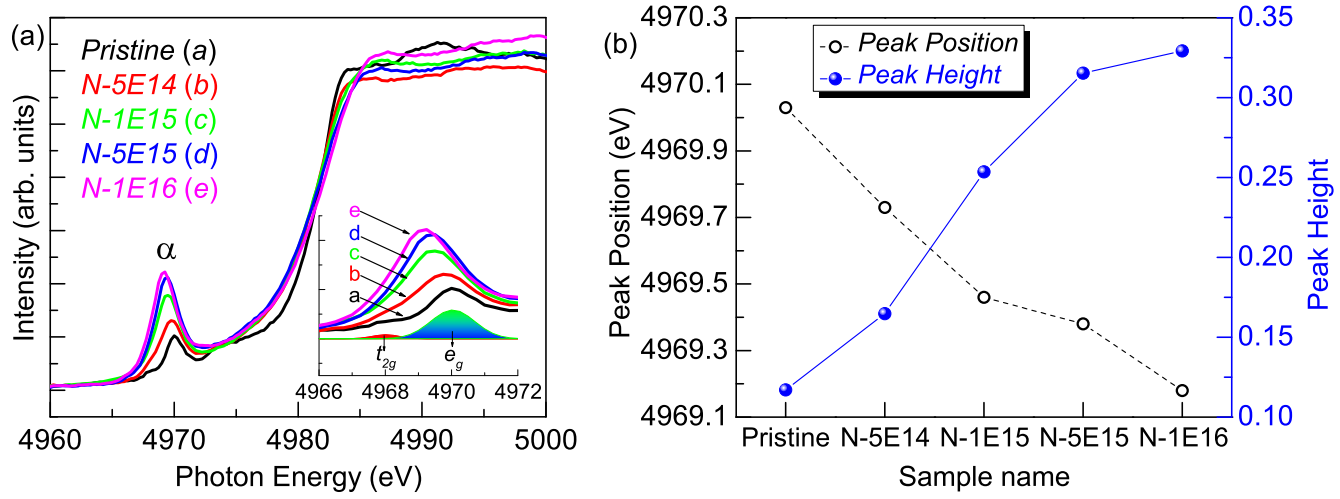

FIG. 4. (a) Ti K-edge spectra of N ion implanted films. Inset shows the pre-edge region, labeled as a, b, c, d, and e corresponding to pristine, N-5E14, N-1E15, N-5E15, and N-1E16, respectively. (b) The variations in the peak position and height of peak α as the function of N ion fluences.

to the fourfold coordinated Ti ions whereas the lower intensity to sixfold geometry of the octahedron [40]. From Fig. 4(b), the position of the peak α shifts towards lower energy side, and its intensity increases with an increase in N ion fluences which indicates a reduction in the coordination number of Ti ions in N ion implanted STO [42]. It has been reported that the amorphous STO has a more intense pre-edge peak and shifts towards lower energy in comparison to crystalline STO [41]. The area under the peak α can be analyzed to estimate the off-center displacement of Ti ions from the center of TiO_6 octahedron [42]. The relation between the off-center displacement d of Ti ion and area under the peak α is related by $A = \frac{\gamma}{3}d^2$ where γ is a constant for a particular perovskite [40–42,44]. From Table III, the increase in intensity and area under the pre-edge peak specifies the increase in off-center displacement of Ti ions.

The chemical shifts of STO films were calculated using the reference compounds of Ti_2O_3 (Ti^{+3}) and single crystal STO (SSTO, Ti^{+4}) by taking the first derivative of Ti K-edge spectra. The average Ti valence states are determined by extrapolation of the energy of Ti K-edge spectra with the standards and are given in Table III along with estimated compositions of the films. This indicates a mixed-valence state of Ti (+3 and +4) with oxygen vacancy surrounding the Ti ions in N ion implanted films. Hence, it is inferred that N-5E14 contains ∼62% and ∼38% of Ti ions in +3 and +4 valence states, respectively. Similarly, both N-1E15 and N-5E15 have ∼77% and ∼23% of Ti ions in +3 and +4 valence states, respectively. The average valence state of Ti ions in pristine and N-1E16 are considered to match with the standard STO and Ti_2O_3, respectively.

The analysis of Ti K-edge spectra of these samples gives extensive information about the changes induced by N ion implantations in the crystal structure and the coordination number of Ti ions. Ti L-edge XANES spectra were recorded in the energy ranges of 440 eV to 490 eV that provide information about the nature of Ti $3d$ orbitals in the electronic structure of STO. These spectra are divided into two regions viz. L_3 and L_2 edge. The L_2 edge appears broader than the L_3 edge due to Coster-Kroning decay [45,46]. In the transition metals, the $2p$ orbitals are split into $2p_{3/2}(L_3)$ and $2p_{1/2}(L_2)$ by spin-orbit interaction and the Ti $3d$ orbitals into t_{2g} and e_g orbitals by crystal field effects [47]. Four absorption peaks are observed corresponding to the following transitions: from $2p_{3/2}$ to $3d$ t_{2g} and $3d$ e_g and from $2p_{1/2}$ to $3d$ t_{2g} and $3d$ e_g orbitals. The L-edge spectra give explicit information on unoccupied $3d$ orbitals which are related to the transition metal ion valency and O vacancies. The normalized Ti $L_{3,2}$-edge spectra of pristine, N-5E14, N-1E15, N-5E15, and N-1E16 are shown in Fig. 5(a). All the peaks were fitted using XPSPEAK4.1 software to determine the accurate peak position, intensity, and area under each peak.

The L_3-edge spectrum of pristine STO film is fitted with two peaks corresponding to t_{2g} and e_g orbitals but one additional peak is needed to fit the spectra of N ion implanted STO films which is assigned to the splitting of $3d$ e_g states into

TABLE III. Peak parameters of pre-edge peak α for all the samples and estimated valency of Ti ions.

Sample name	Peak Position (eV)	Height	FWHM (eV)	Area under the peak	First derivative	Valence state	Composition
Pristine	4970.01	0.1170	1.555	0.1936	4969.7	4	$SrTiO_3$
N-5E14	4969.73	0.1648	1.949	0.3419	4968.9	3.38	$SrTiO_{2.70}$
N-1E15	4969.46	0.2535	2.209	0.5961	4968.7	3.23	$SrTiO_{2.62}$
N-5E15	4969.38	0.3153	2.268	0.7614	4968.7	3.23	$SrTiO_{2.62}$
N-1E16	4969.18	0.3292	2.339	0.8199	4968.4	3	$SrTiO_{2.50}$

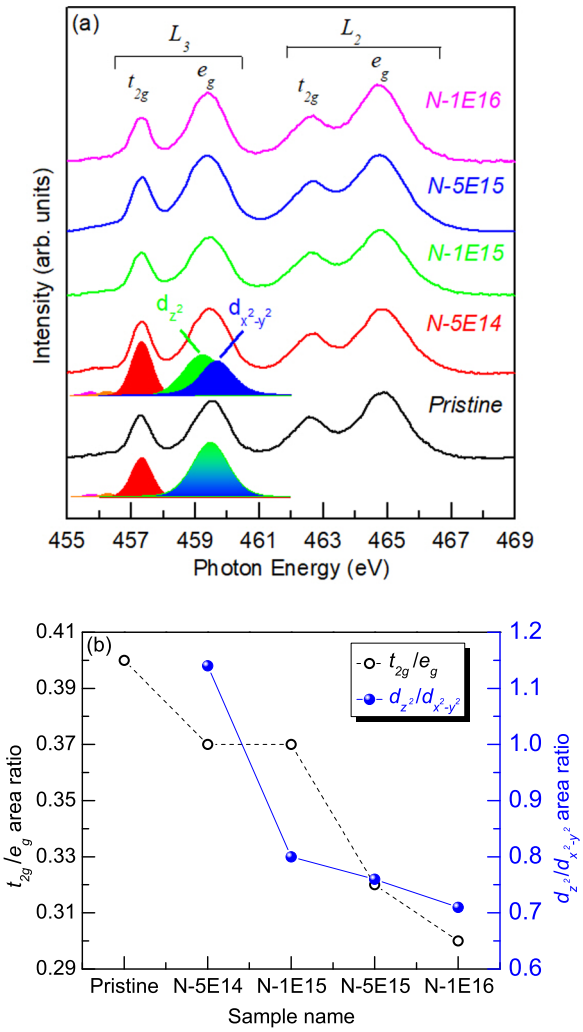

FIG. 5. (a) Ti $L_{3,2}$-edge spectra of pristine and N ion implanted STO films. The deconvoluted L_3-edge spectra under the pristine and N-5E14 are shown to explain the splitting in e_g states. (b) The change in area ratio t_{2g}/e_g and $d_{z^2}/d_{x^2-y^2}$ as a function of N ion fluence calculated for Ti L_3-edge spectra of pristine and N ion implanted STO films.

d_{z^2} and $d_{x^2-y^2}$ orbitals. The ratios of area under the $3d$ t_{2g} and $3d$ e_g orbitals derived peaks, and ratio $d_{z^2}/d_{x^2-y^2}$ are plotted as a function of N ion fluences as shown in Fig. 5(b) and listed in Table IV. The discrepancy in the ratio $d_{z^2}/d_{x^2-y^2}$ implies a distorted noncubic TiO_6 octahedral structure [48]. This can be accredited to a change in the Ti-O bond due

TABLE IV. Area ratios t_{2g}/e_g and $d_{z^2}/d_{x^2-y^2}$ corresponding to Ti L_3 and O K edges for pristine and the N-ion implanted STO films.

		Ti L edge		O K edge	
Sr. no.	Sample	t_{2g}/e_g	$d_{z^2}/d_{x^2-y^2}$	t_{2g}/e_g	$d_{z^2}/d_{x^2-y^2}$
1	Pristine	0.40		0.60	0.43
2	N-5E14	0.37	1.14	0.57	0.35
3	N-1E15	0.37	0.80	0.36	0.34
4	N-5E15	0.32	0.76	0.29	0.30
5	N-1E16	0.30	0.71	0.24	0.20

to variation in the degree of hybridization. The amount of splitting in $3d$ e_g state gradually increases as a function of N ion fluence. Jan *et al.* observed the off-center displacement of Ti ion from the octahedral site which is reflected in the Ti L edge of $Pb_{1-x}Ca_xTiO_3$ (PCT) as splitting in $3d$ e_g orbitals [49]. Mastelaro *et al.* observed that the degree of distortion in the octahedral structure of $Pb_{1-x}La_xTiO_3$ (PLT) decreases on increasing the La doping and less pronounced splitting of $3d$ e_g orbitals in Ti L edges [50]. Therefore, the splitting of $3d$ e_g orbitals into d_{z^2} and $d_{x^2-y^2}$ is a measure of the degree of deviation from octahedral symmetry [50].

The intensity of Ti L_3 edge is proportional to the density of unoccupied states which is the sum of t_{2g} and e_g states [46,48,51]. In principle, the ratio $t_{2g}/(t_{2g}+e_g)$ and $e_g/(t_{2g}+e_g)$ should be 0.6 and 0.4, respectively, for Ti^{+4} since there are no electrons in $3d$ orbitals [52]. These ratios can be also written as t_{2g}/e_g which turns out to be 6/4 (or 3/2). This is a theoretical assumption where all the Ti ions are assumed to be in d^0 state and if only one electron is considered in the calculations ignoring the electron-electron correlation. For octahedral symmetry, the ratio of unoccupied orbitals is 6/4 as t_{2g} and e_g can take six and four electrons, respectively [52]. Kuo *et al.* stated that the intensity of the spectral feature assigned to t_{2g} states is sensitive to the valence state of Ti ion [48]. The more intense t_{2g} feature implies an increase of the oxidation state and thus indicates the presence of Ti^{+4} ($3d^0$) with respect to the TiO_2 system [51]. Janotti *et al.* performed the HSE (Heyd-Scuseria-Ernzerhof) calculation and reported that if one electron is added to the TiO_2 system, it goes to Ti ion occupying the nearest neighbor site to the O vacancy [53]. According to the density functional theory (DFT) calculations by Lin and co-workers, the added one electron has a high probability of occupying the lowest energy state (t_{2g}) of the octahedral symmetry [54]. Hence, in the case of d^1 state, the t_{2g} orbital is filled with one electron being available at the lower energy state. Thus, the ratio t_{2g}/e_g decreases from 6/4 to 5/4. Similarly, for d^2 and d^3 state, the ratio will be 4/4 and 3/4, respectively. Hence, if one considers the ratio t_{2g}/e_g, any change in t_{2g} state (or a charge state of Ti) will be evident [51]. This is due to change in the density of unoccupied $3d$ orbitals. The decrease in the intensity of the t_{2g} peak with an increase in N ion fluence indicates the presence of Ti^{+3} ($3d^1$) in the N ion implanted samples. The t_{2g}/e_g ratio decreases as the content of N increases. This implies that the oxygen vacancies are also increasing with N ion implantation. The Ti L-edge spectra of these films are also compared with an O deficient STO thin film annealed at 750 °C in Ar+H_2(5%) gas flow for 5 h. The t_{2g}/e_g ratio is estimated to be 0.33 for these O deficient films. Thus, the electronic configuration of Ti from the Ti-O bond exhibits a combination of $3d^0$ in Ti^{+4} and $3d^1$ in Ti^{+3} in the ground state [55,56]. However, the pristine film also deviates from the expected value of t_{2g}/e_g ratio. The calculated ratio based on Ti L-edge spectra is 0.4. Wu *et al.* measured Ti L-edge spectra of TiO_2 nanotubes and reported that the t_{2g}/e_g ratio is in a range of ~0.29–0.31 [57]. At first observation, as evident from the RBS study (see SM [29]), the surface layer is found to be $Sr_{0.95}TiO_{2.98}$. Since the thin-film fabrication with perfect stoichiometric composition and uniform thickness is a big challenge, any slight deviation causes change in the value of t_{2g}/e_g ratio [58]. There are some detailed reports

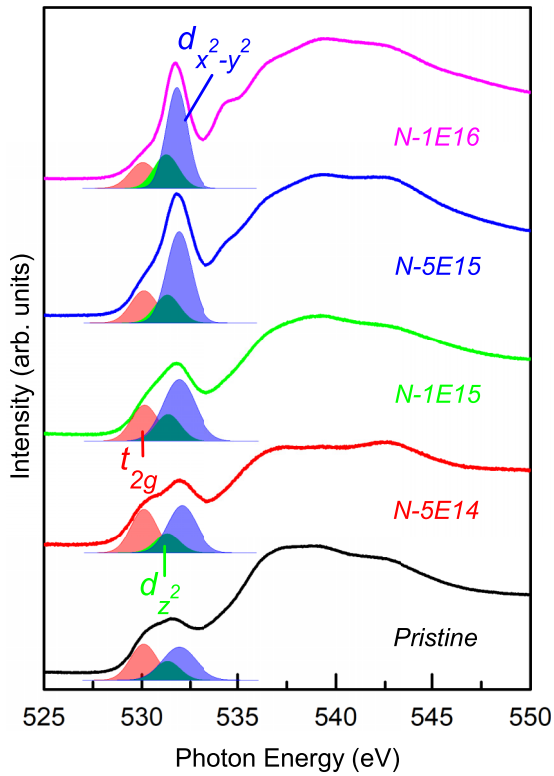

FIG. 6. O K-edge spectra of pristine and N ion implanted STO. The deconvolution of pre-edges are also shown under the corresponding spectra.

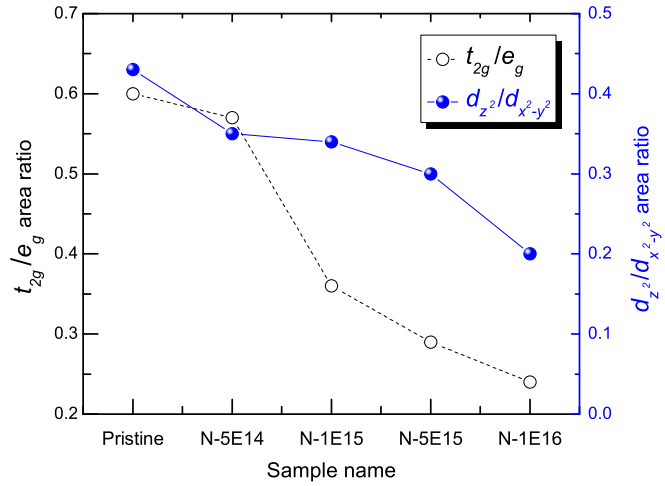

FIG. 7. The change in t_{2g}/e_g and $d_{z^2}/d_{x^2-y^2}$ area ratios as a function of N ion fluence for O K-edge spectra of pristine and N ion implanted STO films.

understanding the Ti L-edge spectra using Multiplet calculations [59,60]. Kroll *et al.* observed that the t_{2g}/e_g ratio does not match with the expected value of 3/2 while considering the spin-orbit coupling and crystal field that fit the experimental spectra [60]. In the crystal field, 3d orbitals split into t_{2g} and e_g, while these states are mixed in the final states through 2p3d Coulomb interaction and within the same symmetry, the intensity is transferred between states [60]. Hence, the final states do not show the expected t_{2g}/e_g ratio. Similarly, Laskowski *et al.*, while calculating the XAS spectra at the L edges of STO by solving the Bethe-Salpeter equation (BSE), also observed that the ratio t_{2g}/e_g is not as expected to be 3/2 [59]. Wu *et al.* performed configuration interaction (CI) cluster calculations for STO to reproduce Ti L-edge spectra and observed that the ratio t_{2g}/e_g increases with an increase in hybridization strength [61]. Hence, the presented Ti L-edge spectra and analysis are in line with the reported multiplet scattering calculations of $SrTiO_3$ [59,60,62–65].

The nature of bonding of O ions with constituent ions (Ti, Sr, and implanted N) was investigated by recording the XANES spectra at O K edge. These spectra are very sensitive to the Ti-O hybridization. Figure 6 shows the XANES spectra at O K edge for pristine, N-5E14, N-1E15, N-5E15, and N-1E16. The prominent spectral features up to 535 eV are assigned to the transitions from O 1s orbitals to hybridized states between O 2p and Ti 3d orbitals and the peaks above 535 eV are the hybridized states between O 2p and Ti 4sp orbitals. To determine the accurate positions and area under the featured peaks, the spectra were fitted using XPSPEAK4.1 software. The pre-edges can be deconvoluted using three peaks which are assigned to 3d t_{2g} and 3d e_g orbitals (d_{z^2} and $d_{x^2-y^2}$) derived peaks. These peaks are separated due to crystal field splitting.

In Fig. 6, the area under the 3d t_{2g} peak is filled with red. The width and asymmetry of the 3d e_g peak suggests the inclusion of two peaks to fit the pre-edge region which is attributed to the splitting in 3d e_g states into d_{z^2} and $d_{x^2-y^2}$. These two peaks are shown by filling the area under the peak with green and blue, respectively. The t_{2g} and e_g peaks arise due to the transitions from O 2p to 3d t_{2g} and 3d e_g orbitals, respectively. The 3d e_g states appear at higher energy and have stronger coupling with O 2p ions than the t_{2g} states because d_{z^2} and $d_{x^2-y^2}$ levels are directed towards O ions. Therefore, 3d e_g states are more sensitive to the deviations in the symmetry of octahedral structure [66]. Hence, the positions of the 3d e_g spectral features of O K edges vary with change in the ion fluence. This can be a consequence of different local environment and ion coordination. The change in the crystal field splitting ($\triangle 3d$) for all the implanted films indicates the variation in the Ti-O distance as a result of change in O 2p-Ti 3d overlap [47]. Also, the O K-edge spectra become sharper after N ion implantation. The sharpness of the peaks derived from the O 2p-Ti 3d hybridized orbitals implies higher order of covalent bonding between the Ti and O atoms [67].

The ratio t_{2g}/e_g decreases gradually with an increase in the N ion fluence. It implies that the 3d t_{2g} states are occupied due to the creation of O vacancies [53–56]. The ratio of area under the d_{z^2} and $d_{x^2-y^2}$ peaks also changes with N ion fluence as shown in Fig. 7 and Table IV. It suggests the existence of O vacancies and mixed valence states of Ti ion [48,51]. Besides, the splitting in the peak, assigned to 3d e_g state, can be attributed to the modifications in O 2p-Ti 3d hybridization states and the distortion in the TiO_6 octahedral structure [48].

IV. DISCUSSION

As evident from TRIM simulations, N ions cause displacements of the target atoms which may result in vacancies

thereof. The knocked-out Ti and O ions possibly occupy the interstitial sites in the octahedra which may be responsible for the observed expansion in interplanar spacing [17]. From the XRD pattern, it is evident that the crystallinity decreases with N ion implantation and amorphization is observed at higher fluences. In the previous study, it is revealed that the presence of O vacancies and N interstitials in the STO thin films induced by low energy N ion implantation cause a split in the XRD reflections and amorphization of the films [17] which can be comprehended by evoking the ion beam interaction with materials.

When an energetic ion passes through a material, it undergoes a series of collisions with the nuclei and atomic electrons of the material. The incident ion loses its energy via two processes mainly (i) elastic collisions with the target nucleus which leads to displacement of the atoms as a whole (nuclear energy loss, S_n) and (ii) inelastic interaction with the electrons that excite or eject the atomic electrons (electronic energy loss, S_e) [30]. Low energy ion interactions are dominated by elastic processes, resulting in the ballistic atomic displacements of the target atoms. This causes radiation damage in the target material. At sufficiently high doses, it results in the crystalline to the amorphous transformation of the irradiated area because of complete disordering in the crystal lattice [68–70]. This amorphization depends on the type of materials, the mass of ion, and ion irradiation conditions [30]. The light mass projectiles create isolated point defects that accumulate to transform crystalline to amorphous structure [71] after certain ion fluence. In the case of heavy ions, dense collision cascades create amorphous pockets which result to transform into the amorphous structure [72]. In the present case, almost complete amorphization is observed with the low energy N ion implantation in N-1E16 STO thin film. Hence, this study focuses on varying ion fluences from 5×10^{14} ions/cm^2 to 1×10^{16} ions/cm^2. Kan *et al.* irradiated STO films with 300 keV Ar^+ ions and reported a thin amorphous layer of few nanometers near the surface [10]. The XRD results are corroborated by XANES studies of Ti K edge. There is an evolution and a shift in the pre-edge position of Ti K edge towards lower energies with an increase in the N ion fluences. This indicates the amorphization of the films, reduction in the coordination number, and a decrease in the valence state of Ti ion (from +4 to +3) [40–42,44]. Both Ti L- and O K-edge spectra depict the modifications due to N ion implantation and the spectral feature assigned to e_g state splits into d_{z^2} and $d_{x^2-y^2}$ orbitals. The splitting in e_g states is an indication of distortion in the crystal structure [50]. This supports the shift in diffraction peak and change in the lattice parameters with N ion fluence. Based on atomic multiplet scattering calculations, Fan *et al.* simulated the Ti L-edge spectra for $ATiO_3$ (Ca, Sr, Ba) system and reported that there is a drastic change in the electronic structure of O ion due to different local environment resulting in a strong hybridization between O ion and A cation [62]. The intensity of $d_{x^2-y^2}$ increases with ion fluence. The decrease in the ratio of t_{2g}/e_g in Ti L and O K edge implies the decrease in density of unoccupied t_{2g} states. Also, the discrepancy in ratio $d_{z^2}/d_{x^2-y^2}$ is a direct indication of lattice distortion and change in Ti-O hybridization.

In the cubic perovskite structure, Ti ion at the body center is surrounded by six O ions situated at the faces of cubic

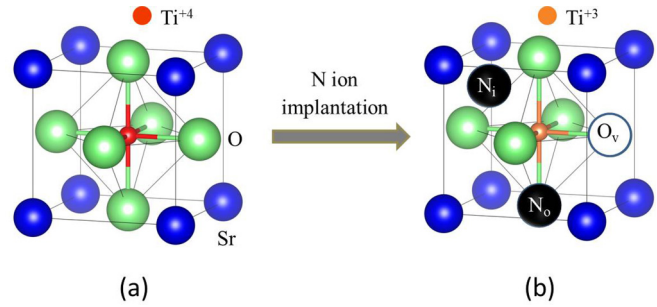

FIG. 8. (a) Cubic perovskite structure of pristine STO and (b) the possible deformation in local atomic structure of STO after N ion implantation.

structure [19,73]. If the O ions are knocked out from their sites, the Ti ions are displaced from their center to stabilize the octahedral structure resulting in off-center displacement and lattice expansion. Kan *et al.* revealed that the presence of O vacancies is responsible for blue emission in STO [10]. The role of N ions is still to be explored to understand the origin of blue-green PL emission. A few studies based on first principle calculations using the DFT have been reported for N doped $SrTiO_3$ and TiO_2 systems [74–76]. In these studies, a few models based on the occupancies of N such as substitutional, interstitial, and oxygen vacancies accompanied by N doping in STO lattice were considered [74–80]. Mi *et al.* reported that the substitutional occupancy is favored in comparison to interstitial and stated that the substitutional N $2p$ localized states lie above the top of O $2p$ valence band (VB) [74,75]. Miyauchi *et al.* performed similar first principle calculations based on DFT considering the substitutional occupancy of N and assumed the band structure being narrowed due to N $2p$ and Ti^{+3} localized states above the VB and below the conduction band (CB), respectively [76]. According to SRIM-TRIM calculation, an increase in ion fluence leads to an increase in vacancies because more number of ions hitting the target results in sputtering of oxygen ions due to its high sputtering yield [30]. In addition to ion beam induced vacancies, N implantation facilitates the formation of oxygen vacancies to maintain the charge neutrality [78]. Thus, the combined effect of ion implantation and N substitution leads to an increase in the number of oxygen vacancies [81–84].

Based on the above results using synchrotron characterization techniques viz. XRD, PL, and XAS, and the existing literature based on first principle calculations using DFT for N doped $SrTiO_3$, and TiO_2 systems, a schematic crystal structure is proposed as shown in Fig. 8. The pristine sample possesses an ideal cubic crystal structure in which Ti^{+4} ion has coordination number of 6 [Fig. 8(a)]. Implantation of N ions creates oxygen vacancies in the lattice [shown as O_v in Fig. 8(b)], which results in +3 valence state of the body-centered Ti ion. The N and O ions possess almost identical radii. Hence, N ion can either substitute O atom (shown as N_o) or occupy the interstitial sites (shown as N_i). There are six O ions located at the face center of STO cubic structure. The probability of occupancy of any O site by N_o depends on the ion implantation conditions like ion species, energy, fluence, current, and the time of exposure to the ion beam

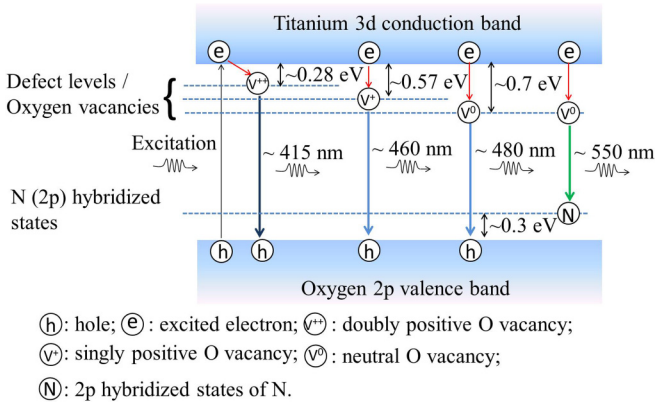

FIG. 9. Schematic diagram of energy levels illustrating the possible mechanisms for observed PL emission.

[11]. Therefore, it is challenging to determine the exact charge state of the O vacancy. To identify the possible transitions, defect levels, and recombination of the electron-hole pair, a schematic diagram of energy levels is proposed as shown in Fig. 9 and discussed as follows. The band gap of STO is of the order of ∼3.3–3.4 eV which arises from the gap between the Ti 3*d* CB and the O 2*p* VB [11]. Xu *et al.* studied the effect of crystallization on the band structure of STO films and proposed an energy band structure for amorphous and crystalline STO [34]. As there is no long-range order in the amorphous STO, tailing localized states appear near the extended VB and CB [34,35]. The bound states corresponding to the O vacancy donor levels also appear near the E_f [10,34,85]. Mitra *et al.* studied the electronic structure of O vacancies in STO and $LaAlO_3$ using HSE hybrid density functional and suggested that the O vacancies can be neutral (V^0), singly positive (V^+), or doubly positive (V^{++}) which create bound states, respectively, at 0.7 eV, 0.57 eV, and 0.28 eV below the CB in the band gap [12,16,85,86]. The implanted N ions form a bound state of hybridized 2*p* orbitals above the top level of the VB [20]. The recombination of excited electrons (in the CB) and the holes (in the VB) through the bound states of doubly positive O vacancies (V^{++}) results in the blue emission at ∼415 nm (A) [5,10], whereas the transitions of the excited electrons through the bound states of singly positive (V^+) and neutral O vacancies (V^0) give emissions at ∼460 nm (B) and ∼480 nm (C), respectively. If the transitions of excited electrons occur through V^0 to the N 2*p* hybridized states or trap levels near the valence band [5,10,20], a green emission appears at ∼550 nm (D). At higher fluences (N-5E15 and N-1E16), the number of singly positive O vacancies increase which contributes to the emission at ∼460 nm. When the O ions are knocked out by N ions, they leave two unbound electrons behind with a neutral O vacancy. On increasing the N ion fluence, we observed that the number of O vacancies having one unbound electron has increased. In any material, there is a limit of creating O vacancies [87]. At higher fluence, the number of implanted N ions increases, and the number of O vacancies approaches the limit. Therefore, to balance the extra negative charge of implanted N ion, an electron is emitted from the neutral O vacancy. However, it is tricky to control this phenomenon as the creation of defects depends on the ion beam current, energy, and fluence, i.e., exposure time to beam [11]. As evident from Fig. 9, a variety of PL emissions are observed in PL spectra through the bound states of O vacancies and N 2*p* states. Hence, N ion implantation proves to be a very efficient technique to make a tunable photoluminescent material for optoelectronics applications.

V. CONCLUSION

STO thin films deposited by RF sputtering were subjected to 100 keV N ion beam to investigate the change in structural, optical, and electronic properties. XRD spectra reveal distortion in the lattice structure and amorphization of films at higher fluences. An intense blue-green emission corresponding to the bound states of O vacancies and implanted N ions are observed in N ion implanted films. This makes the N ion implanted STO a promising material for the future optoelectronics. The XANES at Ti *K* edge show the amorphization of films, change in valency states (from +4 to +3), and reduction in the coordination number of Ti ions. The splitting of 3*d* e_g states into d_{z^2} and $d_{x^2-y^2}$, observed from the Ti *L* and O *K* edges, confirms the distortion in lattice along with its expansion. This study using the synchrotron-based characterization techniques explains the origin of blue-green photoluminescence emission in N ion implanted STO.

ACKNOWLEDGMENTS

Authors are thankful to the Department of Science and Technology, Delhi, India, and Elettra Sincrotrone Trieste, Italy for providing the fund to perform the synchrotron x-ray diffraction measurements at MCX beamline Elettra, Italy corresponding to proposal no. 20175434. Authors thank IUAC scientists, Mr. Kedar Mal for his support in low energy N ion implantation, and Mr. Sunil Ojha and Mr. G. R. Umapathy for RBS measurements. The authors would like to thank Dr. Bing-Ming Cheng, Dr. Sheng-Lung Chou, and Dr. Jen-Iu lo, National Synchrotron Radiation Research Center (NSRRC), Taiwan for their consistent support during the beamtime at TLS-03A1 beamline. Authors are also thankful to NSRRC, Taiwan for XAS measurements at TLS-20A1 and 17C1 beamline. V.K. and A.B. gratefully acknowledge the financial support in the form of fellowship given by UGC Delhi, India, and CSIR Delhi, India, respectively. Authors thank the Department of Science and Technology, India (SR/NM/Z-07/2015) for the financial support and Jawaharlal Nehru Centre for Advanced Scientific Research (JNCASR) for managing the project. C.L.D., K.A., and V.K. would like to acknowledge the MoST Project No. MoST 107-2112-M-032-004-MY3 and Taiwan Experience Education Program (TEEP).

[1] V. Craciun and R. Singh, Appl. Phys. Lett. **76**, 1932 (2000).

[2] H. Inoue, H. Yoon, T. A. Merz, A. G. Swartz, S. S. Hong, Y. Hikita, and H. Y. Hwang, Appl. Phys. Lett. **114**, 231605 (2019).

[3] T. Yajima, M. Minohara, C. Bell, H. Hwang, and Y. Hikita, Appl. Phys. Lett. **113**, 221603 (2018).

[4] R. N. Schwartz, B. A. Wechsler, and L. West, Appl. Phys. Lett. **67**, 1352 (1995).

[5] V. Kumar, S. Choudhary, V. Malik, R. Nagarajan, A. Kandasami, and A. Subramanian, Phys. Status Solidi (a) **216**, 1900294 (2019).

[6] J. E. Ortmann, A. B. Posadas, and A. A. Demkov, J. Appl. Phys. **124**, 015301 (2018).

[7] P. Reunchan, N. Umezawa, A. Janotti, J. T-Thienprasert, and S. Limpijumnong, Phys. Rev. B **95**, 205204 (2017).

[8] Y. Yamada, H. Yasuda, T. Tayagaki, and Y. Kanemitsu, Phys. Rev. Lett. **102**, 247401 (2009).

[9] R. Leonelli and J. L. Brebner, Phys. Rev. B **33**, 8649 (1986).

[10] D. Kan, T. Terashima, R. Kanda, A. Masuno, K. Tanaka, S. Chu, H. Kan, A. Ishizumi, Y. Kanemitsu, Y. Shimakawa, and M. Takano, Nat. Mater. **4**, 816 (2005).

[11] D. Kumar and R. C. Budhani, Phys. Rev. B **92**, 235115 (2015).

[12] D. Liu, Y. Lv, M. Zhang, Y. Liu, Y. Zhu, R. Zong, and Y. Zhu, J. Mater. Chem. A **2**, 15377 (2014).

[13] J. Hanzig, B. Abendroth, F. Hanzig, H. Stöcker, R. Strohmeyer, D. C. Meyer, S. Lindner, M. Grobosch, M. Knupfer, C. Himcinschi, U. Mühle, and F. Munnik, J. Appl. Phys. **110**, 064107 (2011).

[14] M. Zvanut, S. Jeddy, E. Towett, G. Janowski, C. Brooks, and D. Schlom, J. Appl. Phys. **104**, 064122 (2008).

[15] M. Bala, A. Bhogra, S. A. Khan, T. S. Tripathi, S. K. Tripathi, D. K. Avasthi, and K. Asokan, J. Appl. Phys. **121**, 215301 (2017).

[16] J. Lim, H. Lim, and Y. Lee, Curr. Appl. Phys. **19**, 1177 (2019).

[17] V. Kumar, K. Asokan, and S. Annapoorni, in *AIP Conference Proceedings*, Vol. 1837 (AIP Publishing Center, New York, 2017), p. 040040.

[18] B. Santara, P. Giri, K. Imakita, and M. Fujii, J. Phys. Chem. C **117**, 23402 (2013).

[19] M. Yang, J. Oró-Solé, J. A. Rodgers, A. B. Jorge, A. Fuertes, and J. P. Attfield, Nat. Chem. **3**, 47 (2011).

[20] M. Ahmed and G. Xinxin, Inorg. Chem. Front. **3**, 578 (2016).

[21] T. Sun and M. Lu, Appl. Phys. A **108**, 171 (2012).

[22] N. Pathak, S. K. Gupta, P. Ghosh, A. Arya, V. Natarajan, and R. Kadam, RSC Adv. **5**, 17501 (2015).

[23] A. E. Souza, G. T. A. Santos, B. C. Barra, W. D. Macedo Jr., S. R. Teixeira, C. M. Santos, A. M. O. R. Senos, L. Amaral, and E. Longo, Cryst. Growth Des. **12**, 5671 (2012).

[24] L. Gracia, J. Andrés, V. Longo, J. A. Varela, and E. Longo, Chem. Phys. Lett. **493**, 141 (2010).

[25] J. R. Plaisier, L. Nodari, L. Gigli, E. Rebollo San Miguel, R. Bertoncello, and A. Lausi, Acta Imeko **6**, 71 (2017).

[26] L. Rebuffi, J. R. Plaisier, M. Abdellatief, A. Lausi, and P. Scardi, Z. Anorg. Allg. Chem. **640**, 3100 (2014).

[27] H.-C. Lu, M.-Y. Lin, S.-L. Chou, Y.-C. Peng, J.-I. Lo, and B.-M. Cheng, Anal. Chem. **84**, 9596 (2012).

[28] H.-C. Lu, Y.-C. Peng, M.-Y. Lin, S.-L. Chou, J.-I. Lo, and B.-M. Cheng, Anal. Chem. **87**, 7340 (2015).

[29] See Supplemental Material at http://link.aps.org/supplemental/10.1103/PhysRevB.103.024104 for details on SRIM-TRIM calculations, analysis of Rutherford backscattering spectrometry, and deconvoluted photoluminescence spectra, which includes Refs. [30,58] .

[30] J. F. Ziegler, M. D. Ziegler, and J. P. Biersack, Nucl. Instrum. Methods Phys. Res., Sect. B **268**, 1818 (2010).

[31] E. Longo, E. Orhan, F. M. Pontes, C. D. Pinheiro, E. R. Leite, J. A. Varela, P. S. Pizani, T. M. Boschi, F. Lanciotti, A. Beltrán, and J. Andrés, Phys. Rev. B **69**, 125115 (2004).

[32] F. Pontes, E. Longo, E. Leite, E. Lee, J. A. Varela, P. Pizani, C. Campos, F. Lanciotti, V. Mastellaro, and C. Pinheiro, Mater. Chem. Phys. **77**, 598 (2003).

[33] C. S. Kumar, *UV-VIS and Photoluminescence Spectroscopy for Nanomaterials Characterization* (Springer-Verlag, Berlin, Heidelberg, 2013).

[34] K. Xu, M. Yao, J. Chen, P. Zou, Y. Peng, F. Li, and X. Yao, J. Alloys Compd. **653**, 7 (2015).

[35] E. Di Gennaro, U. Coscia, G. Ambrosone, A. Khare, F. M. Granozio, and U. S. Di Uccio, Sci. Rep. **5**, 8393 (2015).

[36] P. Kaur, Kriti, Rahul, S. Kaur, A. Kandasami, and D. P. Singh, Opt. Lett. **45**, 3349 (2020).

[37] B. R. Yakami, U. Poudyal, S. R. Nandyala, G. Rimal, J. K. Cooper, X. Zhang, J. Wang, W. Wang, and J. M. Pikal, J. Appl. Phys. **120**, 163101 (2016).

[38] I. Pelant and J. Valenta, *Luminescence Spectroscopy of Semiconductors* (Oxford University Press Inc., New York, 2012).

[39] B. Ravel and M. Newville, J. Synchrotron Radiat. **12**, 537 (2005).

[40] F. Farges, G. E. Brown, Jr., and J. J. Rehr, Phys. Rev. B **56**, 1809 (1997).

[41] A. I. Frenkel, D. Ehre, V. Lyahovitskaya, L. Kanner, E. Wachtel, and I. Lubomirsky, Phys. Rev. Lett. **99**, 215502 (2007).

[42] A. I. Frenkel, Y. Feldman, V. Lyahovitskaya, E. Wachtel, and I. Lubomirsky, Phys. Rev. B **71**, 024116 (2005).

[43] S. Liu, P. E. Blanchard, Z. Zhang, B. J. Kennedy, and C. D. Ling, Dalton Trans. **44**, 10681 (2015).

[44] F. Farges, G. E. Brown Jr, and J. J. Rehr, Geochim. Cosmochim. Acta **60**, 3023 (1996).

[45] W. Ra, M. Nakayama, W. Cho, M. Wakihara, and Y. Uchimoto, Phys. Chem. Chem. Phys. **8**, 882 (2006).

[46] A. Bhogra, A. Masarrat, R. Meena, D. Hasina, M. Bala, C.-L. Dong, C.-L. Chen, T. Som, A. Kumar, and A. Kandasami, Sci. Rep. **9**, 14486 (2019).

[47] L. Soriano, M. Abbate, A. Fernández, A. R. González-Elipe, and J. M. Sanz, Surface and Interface Analysis **25**, 804 (1997).

[48] H.-W. Kuo, C.-J. Lin, H.-Y. Do, R.-Y. Wu, C.-M. Tseng, K. Kumar, C.-L. Dong, and C.-L. Chen, Appl. Surf. Sci. **502**, 144297 (2020).

[49] J. C. Jan, K. P. Krishna Kumar, J. W. Chiou, H. M. Tsai, H. L. Shih, H. C. Hsueh, S. C. Ray, K. Asokan, W. F. Pong, M.-H. Tsai, S. Y. Kuo, and W. F. Hsieh, Appl. Phys. Lett. **83**, 3311 (2003).

[50] V. R. Mastelaro, P. P. Neves, S. De Lazaro, E. Longo, A. Michalowicz, and J. A. Eiras, J. Appl. Phys. **99**, 044104 (2006).

[51] K.-S. Yang, Y.-R. Lu, Y.-Y. Hsu, C.-J. Lin, C.-M. Tseng, S. Y. H. Liou, K. Kumar, D.-H. Wei, C.-L. Dong, and C.-L. Chen, J. Phys. Chem. C **122**, 6955 (2018).

[52] F. M. F. de Groot, M. Grioni, J. C. Fuggle, J. Ghijsen, G. A. Sawatzky, and H. Petersen, Phys. Rev. B **40**, 5715 (1989).

[53] A. Janotti, C. Franchini, J. Varley, G. Kresse, and C. Van de Walle, Phys. Status Solidi RRL **7**, 199 (2013).

[54] C. Lin, D. Shin, and A. A. Demkov, J. Appl. Phys. **117**, 225703 (2015).

[55] J. H. Richter, A. Henningsson, B. Sanyal, P. G. Karlsson, M. P. Andersson, P. Uvdal, H. Siegbahn, O. Erikkson, and A. Sandell, Phys. Rev. B **71**, 235419 (2005).
[56] P. Le Fevre, J. Danger, H. Magnan, D. Chandesris, J. Jupille, S. Bourgeois, M.-A. Arrio, R. Gotter, A. Verdini, and A. Morgante, Phys. Rev. B **69**, 155421 (2004).
[57] J.-W. Wu, C.-H. Chen, C.-J. Lin, K. Kumar, Y.-R. Lu, S. Y. H. Liou, S.-Y. Chen, D.-H. Wei, C.-L. Dong, and C.-L. Chen, Appl. Surf. Sci. **527**, 146844 (2020).
[58] T. Sarkar, S. Ghosh, M. Annamalai, A. Patra, K. Stoerzinger, Y.-L. Lee, S. Prakash, M. R. Motapothula, Y. Shao-Horn, L. Giordano, and T. Venkatesan, RSC Adv. **6**, 109234 (2016).
[59] R. Laskowski and P. Blaha, Phys. Rev. B **82**, 205104 (2010).
[60] T. Kroll, E. I. Solomon, and F. M. de Groot, J. Phys. Chem. B **119**, 13852 (2015).
[61] M. Wu, H. L. Xin, J. Wang, X. Li, X. Yuan, H. Zeng, J.-C. Zheng, and H.-Q. Wang, J. Synchrotron Radiat. **25**, 777 (2018).
[62] W. Fan, Y. Song, J. Bi, Y. Pei, R. Zhang, and Y. Cao, AIP Adv. **9**, 065213 (2019).
[63] G. Panchal, R. Choudhary, S. Yadav, and D. Phase, J. Appl. Phys. **125**, 214102 (2019).
[64] J. R. L. Mardegan, D. V. Christensen, Y. Z. Chen, S. Parchenko, S. R. V. Avula, N. Ortiz-Hernandez, M. Decker, C. Piamonteze, N. Pryds, and U. Staub, Phys. Rev. B **99**, 134423 (2019).
[65] F. De Groot and A. Kotani, *Core Level Spectroscopy of Solids* (Boca Raton, FL, 2008).
[66] P. Nachimuthu, S. Thevuthasan, E. M. Adams, W. J. Weber, B. D. Begg, B. S. Mun, D. K. Shuh, D. W. Lindle, E. M. Gullikson, and R. C. Perera, J. Phys. Chem. B **109**, 1337 (2005).
[67] A. Braun, K. K. Akurati, G. Fortunato, F. A. Reifler, A. Ritter, A. S. Harvey, A. Vital, and T. Graule, J. Phys. Chem. C **114**, 516 (2010).
[68] S. Hooda, B. Satpati, T. Kumar, S. Ojha, D. Kanjilal, and D. Kabiraj, RSC Adv. **6**, 4576 (2016).
[69] W. Jiang, H. Wang, I. Kim, I.-T. Bae, G. Li, P. Nachimuthu, Z. Zhu, Y. Zhang, and W. J. Weber, Phys. Rev. B **80**, 161301(R) (2009).
[70] R. A. Kelly, J. D. Holmes, and N. Petkov, Nanoscale **6**, 12890 (2014).
[71] J. R. Dennis and E. B. Hale, J. Appl. Phys. **49**, 1119 (1978).
[72] L. Howe and M. Rainville, Nucl. Instrum. Methods **182**, 143 (1981).
[73] S. Fuentes, R. Zarate, E. Chavez, P. Munoz, D. Díaz-Droguett, and P. Leyton, J. Mater. Sci. **45**, 1448 (2010).
[74] Y. Mi, S. Wang, J. Chai, J. Pan, C. Huan, Y. Feng, and C. Ong, Appl. Phys. Lett. **89**, 231922 (2006).
[75] Y. Mi, Z. Yu, S. Wang, X. Gao, A. Wee, C. Ong, and C. Huan, J. Appl. Phys. **101**, 063708 (2007).
[76] M. Miyauchi, M. Takashio, and H. Tobimatsu, Langmuir **20**, 232 (2004).
[77] A. K. Rumaiz, J. Woicik, E. Cockayne, H. Lin, G. H. Jaffari, and S. I. Shah, Appl. Phys. Lett. **95**, 262111 (2009).
[78] M. Batzill, E. H. Morales, and U. Diebold, Chem. Phys. **339**, 36 (2007).
[79] H. Shen, L. Mi, P. Xu, W. Shen, and P.-N. Wang, Appl. Surf. Sci. **253**, 7024 (2007).
[80] R. Asahi, T. Morikawa, T. Ohwaki, K. Aoki, and Y. Taga, Science **293**, 269 (2001).
[81] J. LaGraff, G. Pan, and K.-N. Tu, Physica C **338**, 269 (2000).
[82] O. Lobacheva, Y. Yiu, N. Chen, T. Sham, and L. Goncharova, Appl. Surf. Sci. **393**, 74 (2017).
[83] P. Sudhagar, K. Asokan, E. Ito, and Y. S. Kang, Nanoscale **4**, 2416 (2012).
[84] C. Liu, X. Zu, and W. Zhou, J. Phys. D **40**, 7318 (2007).
[85] C. Mitra, C. Lin, J. Robertson, and A. A. Demkov, Phys. Rev. B **86**, 155105 (2012).
[86] R. Astala and P. Bristowe, Modell. Simul. Mater. Sci. Eng. **9**, 415 (2001).
[87] R. Perez-Casero, J. Perriere, A. Gutierrez-Llorente, D. Defourneau, E. Millon, W. Seiler, and L. Soriano, Phys. Rev. B **75**, 165317 (2007).